Computational fracture analysis of screw-bone interaction in a patient-specific vertebra model

Leonardo Molinari[a], Cristina Falcinelli[a], Alessio Gizzi[a,*], Alberto Di Martino[b,c]

[a] *Department of Engineering, Campus Bio-Medico University of Rome, Via A. del Portillo 21, 00128 Rome, Italy*
[b] *Department of Biomedical and Neuromotor Science DIBINEM, University of Bologna, Bologna, Italy*
[c] *1st Orthopaedic and Traumatologic Clinic, IRCCS Istituto Ortopedico Rizzoli, Bologna, Italy*

Abstract

We propose a novel computational approach of fracture analysis in the human vertebra comparing the biomechanical effects of screw-bone interaction in the lumbar spine. We considered a CT-based three-dimensional FE model of bilaterally instrumented L4 vertebra virtually implanting pedicle screws according to clinical guidelines. Nine screws trajectories were selected from the combination of three craniocaudal and mediolateral angles, thus investigated through extensive computational analyses. Bone was modelled as an elastic material with element-wise inhomogeneous material properties fine-tuned on CT data. In particular, we implemented a custom algorithm to identify the thin cortical layer correctly from CT images ensuring reliable material properties in the computational model. Physiological motion (i.e. flexion, extension, axial rotation, lateral bending) was further accomplished by simultaneously loading the vertebra and the implant. We simulated local progressive damage of the bone by using a quasi-static force-driven incremental approach and considering a stress-based fracture criterion. Ductile-like and brittle-like fractures were found. Statistical analyses show significant differences comparing screws trajectories and averaging the results among six loading modes. We identified the caudomedial trajectory as the least critical case, thus safer from a clinical perspective. Medial and craniolaterally oriented screws, instead, entailed higher peak and average stresses, though no statistical evidence classified such loads as the most critical scenarios.

Keywords: Finite element analysis, Vertebra biomechanics, Bone fracture, Patient-specific modeling, Statistical analysis.

1. Introduction

Spinal fusion is a surgical technique used to fuse two or more vertebrae into a single, solid bone; it is performed to eliminate a painful motion or to restore stability to the spine [1]. At the lumbar spine, it is most commonly performed by inserting pedicle screws (screw fixation) connected to rods to give primary stability to the spinal construct, while the biological fusion process takes place [2]. At present, percutaneous screw fixation has become extremely common to minimise injury to the soft tissue and muscles around the spine [3, 4]; however, in both open and minimally invasive surgeries screw trajectory should follow the same rules. Loosening and breakage of pedicle screw are among the most common instrumentation related complications after surgery and may occur due to the presence of excessive stress concentrations causing implant failure [5]. Screw loosening occurs up to 15 % in non-osteoporotic patients treated with rigid systems and even higher in osteoporotic patients [6]. Screws positioning and angulation have been shown to significantly influence the screw-bone load mechanism, providing a convenient stress distribution thus extensively investigated to reduce the occurrence of failure [7, 8].

*Corresponding author: a.gizzi@unicampus.it

Studying the biomechanical response of the vertebra-screw complex requires Finite Element (FE) modelling and Analysis (FEA). In particular, FEA has been used to investigate failure and implants' effects in vertebra and spine models. Single vertebra segment computational models, for example, investigated failure strength levels, patterns, and location initiation [9, 10]. FEA of implants was mainly employed to examine load transfer mechanisms within a screw/vertebra complex, and the effect of design factors of pedicle screws (e.g pitch length, major diameter, thread profiles, and geometry) [11, 12]. However, only a few studies have been identified involving FEA of spine computational models considering screws insertion angles as critical parameters. Matsukawa et al. [13] compared the traditional trajectory to the cortical bone trajectory, proposed by Santoni et al. [7], demonstrating its superiority in terms of increased fixation strength and biomechanical stiffness under multidirectional loading. Hussain et al. [8] studied the effects of screw angle in the sagittal plane in cervical spine fixation. Newcomb et al. [14], using a patient-specific model, analysed the variation of pedicle screw orientations in the axial and sagittal planes, highlighting effects on peak stresses during loading. Besides, a single left screw was employed in the study. To the best of authors' knowledge, no published studies investigated fracture in instrumented vertebrae considering the variation of pedicle screws orientation.

In the present work, we propose a patient-specific three-dimensional (3D) FE model of human L4 vertebra, bilaterally instrumented with pedicle screws. Our case study stems from CT images routinely recorded in the clinical practice at the Department of Orthopaedics and Trauma Surgery, Campus Bio-Medico University Hospital. At first, we introduced an ad hoc filtering such to correctly detect the thin cortical layer from CT images, preventing deleterious Young's modulus values on the outer surface of the model. Then, we investigated nine different screws combinations, by varying the screws insertion angles in craniocaudal and mediolateral directions conducting a vast computational campaign. We simulated 54 computational models gradually loading pedicles and articular facets multiaxially and by applying physiological boundary conditions. We further imposed incremental loads in conjunction with a finite element-based fracture law, describing the progressive weakening of the bone up to complete fracture of the vertebra. Intending to quantitatively highlight the role of screws orientation on the biomechanical response of the vertebra, we finally performed an extensive statistical analysis comparing and contrasting 13 field variables thus providing a specific indication of the most critical insertion scenarios. Our results show, in particular, two possible fracture mechanisms, a ductile-like and a brittle-like, in conjunction with a critical combination of screw angles.

The paper is organized as follows. In Section 2, we describe image segmentation, CT-based material modelling, boundary conditions, and numerical methods. In Section 3 we provide numerical convergence and computational results along with an extended comparison of the different screws combinations and loading modes, supported by multiple statistical analyses. In Section 4 we discuss model reliability and draw conclusions, limitations, and future perspectives.

2. Methods

In this section, we provide the methodology adopted to generate a subject-specific CT-based 3D FE model of L4 vertebra, bilaterally instrumented with pedicle screws. A spinal CT scan (SOMATOM Sensation 64 Siemens Healthineers AG, Munich, Germany) of a 49-year-old female patient without pathologies affecting the spinal bone quality was used for the current study. The imaging was performed for a recent trauma, but the scan was negative for fractures. The images were acquired without a calibration phantom, using the following parameters: 120 kVp, 489 mA, 0.8418×8418 mm pixel size and 1 mm slice thickness. Data were anonymized so that the identification of the patient was not possible.

2.1. Geometry

In Fig. 1(a) we show the three-dimensional human vertebra geometry segmented from CT data and obtained by using a semi-automatic level-set algorithm with a subsequent manual refinement[1]. After applying an

[1]ITK-SNAP 3.8.0, University of Pennsylvania, Phildelphia, PA, USA.

additional smoothing[2], we partitioned the geometry model such to obtain articular facets, bottom and top endplates for loading application (see Fig. 1(b)). Screw insertion (see Fig. 1(c)) was finally introduced as described below.

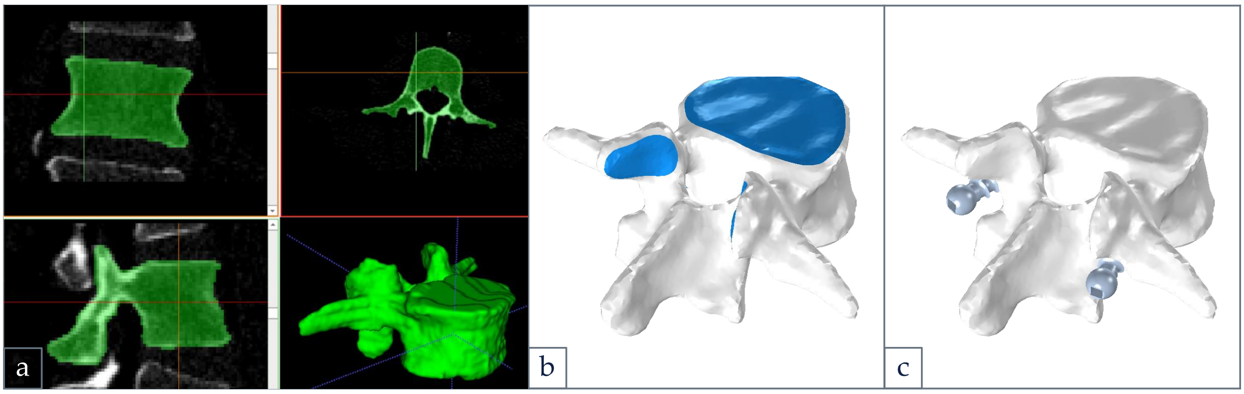

Fig. 1. Procedure for geometry creation: segmentation from CT images (a); smoothing and manual partitioning of articular facets, top and bottom endplates (b); virtual implantation of screws and assembly creation (c).

We designed a custom CAD geometry $\varnothing 6.5 \times 40$ mm cylindrical fully threaded non-cannulated pedicle screw (based on commercial polyaxial pedicle screw features), with a minor diameter of 4.3 mm, a thread pitch of 3 mm and a thread depth of 1.1 mm (see Fig. 2). Though the original threaded profile is usually simplified to reduce the computational cost of FE analyses [15, 16], in this work we opted to maintain sharp interfaces in the computational model. Based on a preliminary computational analysis, we observed that the chosen methodology provides more reliable stress and strain distributions than the simplified approach, without a significant increase in the computational cost.

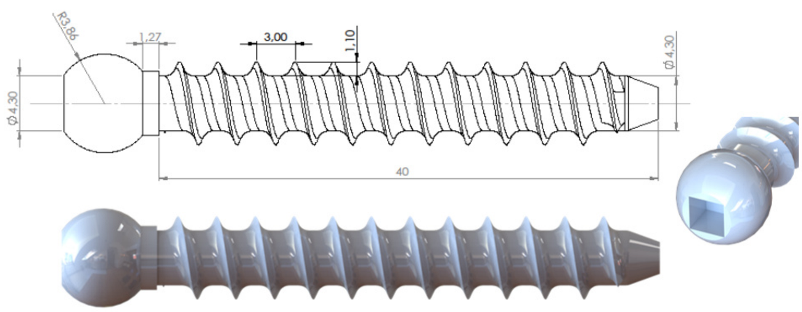

Fig. 2. Fully threaded non-cannulated pedicle screw used in the FE analysis with dimensions: 40 mm (length), 6.5 mm (major diameter), 4.3 mm (minor diameter), 3 mm (thread pitch), and 1.1 mm (thread depth).

We identified screws insertion points to comply with the clinical indications and simulate a transpedicular convergent trajectory, which is considered the most common in the surgical practice. Such a feature was considered fixed for the different combinations of insertion angles tested in the present study. Screws were inserted to a depth of 30 mm and we obtained different trajectories by rotating both screws simultaneously around their insertion points in the mediolateral (transverse) and craniocaudal (sagittal) directions (see Fig. 3). The configuration obtained inserting the screws without any rotation will be referred to as the neutral one. Asymmetrical combinations were not taken into account such to reduce the overall number of configuration tests. We analysed a total of 9 different trajectories, as the result of the combination of 3

[2]Meshmixer 3.5, Autodesk Inc., San Rafael, CA, USA.

craniocaudal $(-5, 0, 5)^{\circ}$ and 3 mediolateral $(-5, 0, 5)^{\circ}$ insertion angles. Considering the neutral configuration as the reference one, we adopted the following convention: in the craniocaudal direction, we assumed positive angles (+5) as cranial and negative angles (-5) as caudal; in the mediolateral direction, we assumed positive angles (+5) as lateral and negative angles (-5) as medial (see Fig. 3(b)). The actual limit angles were defined to prevent any breaching of the cortical layer.

Once the screws were properly positioned, boolean subtraction was performed to simulate the bone removal and the screws implant (see Fig. 1(c)). Thereafter, the hollowed L4 and screws models were imported within the FE simulation environment Comsol Multiphysics[3] and discretised with 10-node tetrahedral elements (see Fig. 3(a)). The automatic mesh function ensures that the built volumetric mesh is congruent, i.e, it makes the nodes of the triangles from different structures to correspond at the intersecting locations. This is an essential requirement to guarantee that the forces are properly transmitted from one structure to the other, in a complex assembly. We selected the maximum element size for the vertebra according to a preliminary convergence analysis (Section 3.1). The minimum element size was set as half of the maximum value, to make the FE discretization as uniform as possible. Concerning the screws, we used element dimensions as half the size of the bone ones. Such a choice ensures a finer screw-bone interface and guarantees numerical accuracy as discussed below.

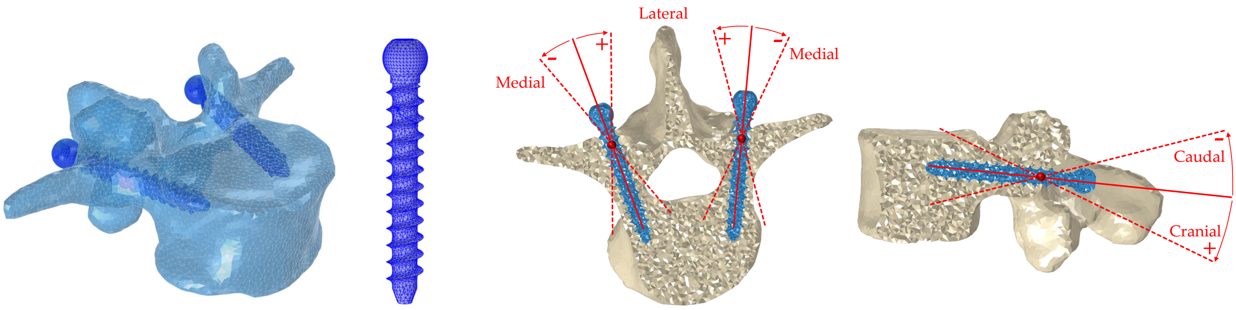

(a) (b)

Fig. 3. (a) Unstructured tetrahedral mesh for the instrumented vertebra and pedicle screw geometry model. (b) Transverse and sagittal mid-sections of the volume mesh indicating the convention used for craniocaudal and mediolateral angles.

2.2. Constitutive modelling and material properties identification

We modelled bone as an isotropic heterogeneous linear elastic material. Heterogeneous element-wise material properties were derived from CT images using a customized Matlab procedure. We first derived Hounsfield Unit (HU) values from biomedical CT data converting the grayscale into apparent (ρ_{app}) and ash (ρ_{ash}) densities. Then, we derived Young's modulus E and yield stress σ_{yield} values from the corresponding density values by using empirical relations as described in the following. The negligible influence of bone Poisson's ratio on the FE analysis outcome is widely documented in the literature [17, 18]. On such a basis, we assumed a uniform constant value of $\nu = 0.3$ [10, 12].

Remark. It is important to note that we assigned local mechanical properties by using the uninstrumented vertebra model (i.e before the insertion of screws). If the instrumented version was used, the filtering procedure would lead to an overestimation of the material properties at the bone-screw interface.

First, we imported the CT data and identified the ROI containing the L4 vertebra. Since the cortical shell in the vertebra is thinner than the clinical CT scan resolution (< 500 µm [19, 20]), we implemented an *ad hoc* identification algorithm to detect the physiological boundaries of the cortical layer preventing detrimental Young's modulus values (see Section 2.2.1). The filtered HU was then linearly interpolated over the mesh

[3]Comsol 5.5, COMSOL, Stockholm, Sweden.

nodes. Linear regression was performed to determine the ρ_{app} − HU relationship. Since no phantom was included in the CT acquisition, a phantomless calibration approach was implemented [17, 21, 22, 23]. In detail, we correlated ρ_{app} to HU imposing $\rho_{app} = 0$ for HU = 0 (water), and assigning $\rho_{app} = 1.9$ [g/cm^3] to the maximum of HU after filtering (cortical bone [24]), equal to 1109. Pointwise negative values of the density were set to $\rho_{app} = 0$ [g/cm^3] to avoid numerical instabilities and unphysical behaviors. Accordingly, we used relationship (a) indicated in Table 1.
As pointed out by Yosibash et al. [25], there is not a straightforward value of HU discriminating between trabecular and cortical bone. In the present work, we assumed [26, 27, 28]:

$$\begin{cases} \text{Trabecular bone:} & \text{HU} < 700, \quad \rho_{app} < 0.8\,[\text{g/cm}^3] \\ \text{Cortical bone:} & \text{HU} \geq 700, \quad \rho_{app} \geq 0.8\,[\text{g/cm}^3] \end{cases}$$

Also, Jones et al. [29] highlighted that there is still no consensus on the most suitable relationship to derive Young's modulus from apparent density. For vertebrae, several relationships have been obtained from mechanical testing of trabecular specimens. Some authors have adopted a single conversion relation for both trabecular and cortical bone supported by the idea that the cortical layer in the spine is a form of condensed trabecular bone. Nevertheless, we performed a preliminary analysis involving multiple relationships observing that a single functional conversion is not the best strategy in our case. In particular, using only one relationship we obtained values for Young's modulus in the cortical layer of vertebral body ($3 \div 6$ [GPa]), not in line with the literature [24, 30].
Accordingly, in the present work, we implemented a different approach. As reported in Tab. 1(b), we adopted the density-elasticity relationships E^T for trabecular bone proposed by Morgan et al. [26] and a custom-made functional form for cortical bone (E^C). The proposed strategy leads to a stiffness range of ($0 \div 3000$) [MPa] for trabecular and ($12 \div 14$) [GPa] for cortical bone. Subsequently, yield stress was evaluated as a function of ρ_{ash}. The latter was derived from ρ_{app} following the approach by Keyak et al.[31], i.e. Tab. 1(c). Conversion rules (d) from Table 1 were considered for compressive yield stress, σ^c_{yield}, [31, 32], where the threshold discriminating among trabecular and cortical bone corresponds to $\rho_{ash} = 0.317$ [g/cm^3]. The resulting ranges of compressive yield stresses was then ($0 \div 19$) [MPa] for trabecular and ($19 \div 140$) [MPa] for cortical bone. Tensile yield stress σ^t_{yield} was assumed as a linear function of the compressive yield stress, as stated in Tab. 1(d). A constant value of $E = 10^{-6}$ MPa and $\sigma^c_{yield} = 10^{20}$ MPa were assigned to elements with $\rho_{ash} = 0$ [g/cm^3]. The material properties obtained, fell within the ranges of physiological variability reported in the literature [12, 24, 30].
As it will be clarified in Section 2.3.1, we also tested a strain-based fracture criterion adopting constant compressive and tensile yield strains ($\epsilon^c_{yield} = 1.04\%$, $\epsilon^t_{yield} = 0.74\%$ [28, 33, 34]).

Table 1
Empirical relations employed to derive material properties from CT data. In the following, $(\bullet)^c$ and $(\bullet)^t$ stand for compressive and tensile loading, while $(\bullet)^C$ and $(\bullet)^T$ identify trabecular and cortical bone domains, respectively.

		Empirical relation	**Range**
(a)	HU to ρ_{app}	$\rho_{app} = 1.9\,\text{HU}/1109$	$0 \div 1.9$ [g/cm^3]
(b)	ρ_{app} to E	$E^{\text{T}} = 4730\,{\rho_{app}}^{1.56}$ $E^{\text{C}} = -892.5\,{\rho_{app}}^{-2.491} + 14360$	$0 \div 3000$ [MPa] $12 \div 14$ [GPa]
(c)	ρ_{app} to ρ_{ash}	$\rho_{ash} = 0.551\,\rho_{app} - 0.00478$	$0 \div 1.04$ [g/cm^3]
(d)	HU to σ_{yield}	$(\sigma^c_{yield})^{\text{T}} = 114\,{\rho_{ash}}^{1.88}$ $(\sigma^c_{yield})^{\text{C}} = 137\,{\rho_{ash}}^{1.72}$ $\sigma^t_{yield} = 0.8\,\sigma^c_{yield}$	$0 \div 19$ [MPa] $19 \div 140$ [MPa] $0 \div 112$ [MPa]

Finally, pedicle screws were modelled as linear elastic isotropic materials, made of TI-6Al-4V (UNS R56400). Young's modulus and Poisson's ratio were assigned as 110 GPa and 0.4, respectively.

2.2.1. *Artefacts Removal*

We developed a custom algorithm of artefact removal to identify the thin cortical layer from CT images correctly. The results of the removal strategy are shown in Fig. 4. Multiple views of the computational domain, before and after the filtering, underline the reliability of the method. In particular, Fig. 4(a) shows predominantly blue colour (low stiffness) on the boundary of the geometry model, thus corresponding to non-physiological stiffness values. However, Fig. 4(b) highlights the expected physiological layer of cortical bone, e.g. red color (high stiffness), providing the correct stiffness values.

Firstly, voxels outside the vertebra domain were identified. Therefore, we derived a constant value of HU = 923 as the mean of HU belonging to cortical bone (HU $\geq$ 700) and assigned it to previously marked voxels. Such an assignment has been adopted to prevent any influence of adjacent soft tissues on the CT data interpolation, which ultimately entails wrong material identification. Eventually, a moving average filter was computed with a $5 \times 5 \times 5$ grid size of the convolution kernel, selected after preliminary comparative analysis.

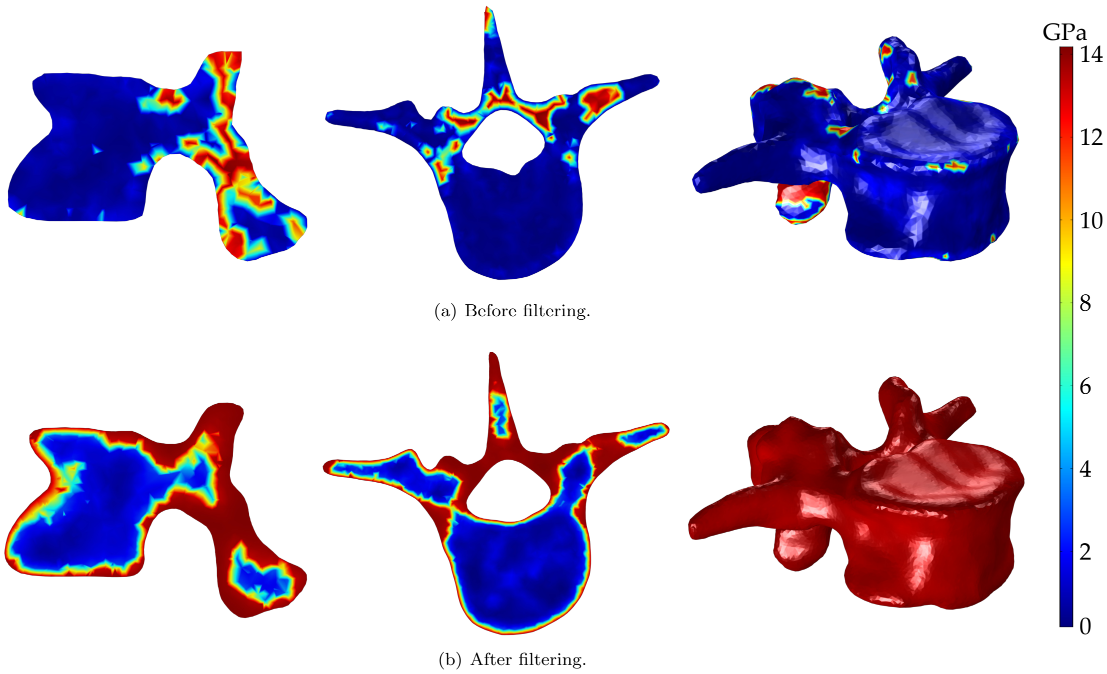

Fig. 4. Uninstrumented L4 model before (a) and after (b) filtering. Panel (b) highlights the outer cortical layer with physiological stiffness values.

2.3. *Boundary conditions*

Validated boundary conditions for extended spine models are available in the literature [35], though not suitable for the present model addressing loads in single vertebral structures. According to a vast review of the studies involving instrumentation of single vertebrae, usual loadings assumptions conceive a force applied to the implant, while the vertebral body is fixed, or vice versa [12, 13, 14]. In this work, we proposed a combined approach to mimic physiological motion, by simultaneously loading the vertebra and the implant. A detailed visual description of the multiple loadings applied is provided in Fig. 5.

We analysed six loading modes reproducing different body positions: flexion (F), extension (E), left (counterclockwise) and right (clockwise) axial rotation (LAR, RAR), left and right lateral bending (LLB, RLB). The inferior endplate of the vertebra was considered fully constrained. We assumed that 80% of the total applied load acts on the vertebra while the remaining 20% on the screws. Also, we included the load sharing contribution of the spinal facet joints [36]. Specifically, the compressive force applied to the vertebra was distributed 70% on the superior endplate (F_{vertebra}), and 30% on the articular facets ($F_{\text{articular}}$).

The load transferred to the implant was applied to the screw heads in different directions, depending on the analysed loading condition (see Fig. 5(b)). A uniform moment of 4.7 Nm [37] was applied along the three principal axes for the different tested conditions (Fig. 5(a)). The centre of rotation was assumed as the centre of the L5-S1 intervertebral disc. The screw-bone interface was simulated as a perfect bonded connection, as reported in previous works [12, 38, 39]. This assumption is supported, in particular, by the use of Ti-6Al-4V screws. The osseointegration properties of titanium and its alloys are extensively documented in the literature [40, 41, 42], especially when combined with biomimetic design and substrate-based surface modification of orthopaedic implants.

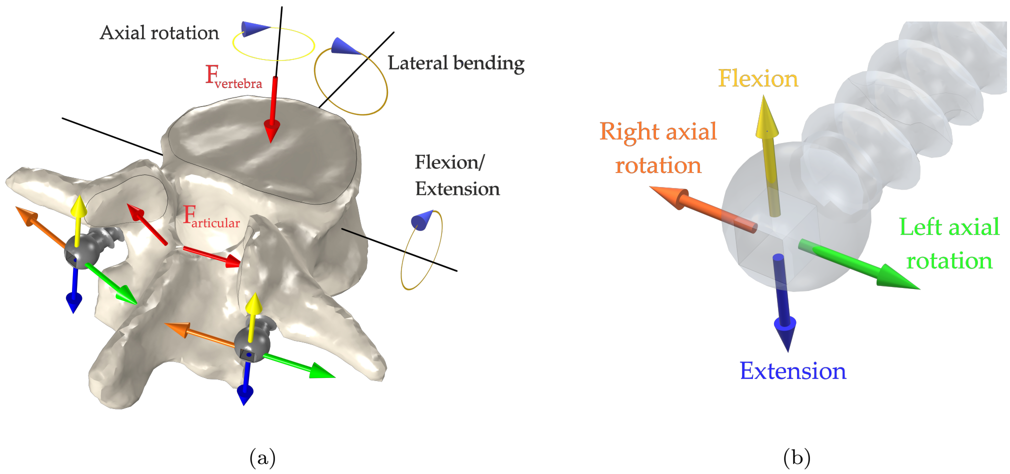

Fig. 5. Boundary conditions applied on the vertebra and the screw achieving multidirectional motion. Moment and compressive loads applied to the screw-vertebra complex are shown. The total applied load is distributed among the vertebral body ($F_{vertebra}$), the articular facets ($F_{articular}$), and the screw heads along with different directions (b): upward for flexion (yellow), downward for extension (blue), to the right for LAR (green) and to the left for RAR (orange). RLB is obtained by applying an upward and a downward force to the left and right screws, respectively (complementarily in the case of LLB).

2.3.1. Fracture criterion and degradation rule

The literature proposes a variety of failure criteria, often not consistent among them, i.e., maximum principal stress criterion or maximum principal strain criterion [21]. The maximum principal stress theory states that failure will occur when the maximum normal stress in any direction equals or exceeds either the tensile or compressive yield strength in the uniaxial tensile test. In particular, tensile and compressive failure conditions read as follows:

$$\begin{cases} \sigma_{max} \geq \sigma^t_{yield} \\ \sigma_{min} \geq \sigma^c_{yield} \end{cases} \qquad \begin{cases} \sigma_{max} = \max\limits_{\{i=1,2,3\}} (0, \sigma_i) \\ \sigma_{min} = -\min\limits_{\{i=1,2,3\}} (0, \sigma_i) \end{cases} \tag{1}$$

with σ^t_{yield} and σ^c_{yield} being non-negative density-based yield stresses defined in Section 2.2, while σ_{max} and σ_{min} being non-negative local stress values defined in terms of principal stresses σ_i, $i = 1, 2, 3$.
The maximum principal strain theory states that failure will occur when the maximum normal strain or the maximum principal strain equals exceeds the strain at the tensile yield point in either simple tension or compression. In particular, tensile and compressive failure conditions read as follows:

$$\begin{cases} \epsilon_{max} \geq \epsilon^t_{yield} \\ \epsilon_{min} \geq \epsilon^c_{yield} \end{cases} \qquad \begin{cases} \epsilon_{max} = \max\limits_{\{i=1,2,3\}} (0, \epsilon_i) \\ \epsilon_{min} = -\min\limits_{\{i=1,2,3\}} (0, \epsilon_i) \end{cases} \tag{2}$$

with ϵ^t_{yield} and ϵ^c_{yield} being non-negative constant compressive and tensile yield strains defined in Section

2.2 ($\epsilon^c_{yield} = 1.04\%$, $\epsilon^t_{yield} = 0.74\%$), while ϵ_{max} and ϵ_{min} being non-negative local stress values defined in terms of principal strains ϵ_i, $i = 1, 2, 3$.
The selection of fracture criteria is still an open problem in the field of bone biomechanics. Fundamentals of bone biomechanics as well as experimental-numerical comparisons indicate that bone fracture occurs through a strain-controlled failure, suggesting the adoption of strain-based criteria [43]. However, the use of stress-based criteria [34, 44, 45] seems to prevail on strain-based ones [9, 46] to predict fracture risk in bone. For the sake of completeness, we implemented both the maximum principal strain and the maximum principal stress criterion, opting for the latter as a result of a preliminary numerical analysis. Specifically, in terms of fracture, both criteria provided good agreement with experimental data [9, 10, 47, 48, 49, 50], with a slight overestimating ($6 \div 7$ kN) of the strain-based criterion.
However, we found that the fracture type was decisive in the final choice of the criterion. The stress-based criterion was mainly associated with a vertebral compression fracture. The strain-based, regardless of the loading mode, systematically predicted a bilateral pedicle fracture, which is extremely rare in the absence of previous spinal surgery or spondylotic changes in the spine [51].

Degradation rule. In the present work, we aimed at numerically simulating bone loss after the failure of the vertebra. Accordingly, we implemented a simple degradation rule consisting of setting Young's modulus of damaged elements to 10^{-6} MPa, once the fracture criterion was satisfied. Thereby, we assume the evolution of fracture through an update of material properties (see the next section for details), while geometry remains fixed.

Remark. It is important to note that the implementation of contact mechanics between fracture surfaces would likely lead to mesh penetration and model convergence issues during the solution [52]. Accordingly, we did not consider such a modelling option in the present work.

2.4. Numerical procedure

The vertebral fracture was simulated using a custom-built Matlab algorithm integrated with the COMSOL Multiphysics FEM solver. We provide the iterative procedure in Fig. 6 that is applied to each screw combination under all the loading conditions described in Section 2.3.

Algorithm 1 Numerical procedure

```
Setup Model
Convergence ← True
i ← 1
while Convergence = True do
    Compute solution at Step i
    if Solution converges then
        if Local failure then
            E_failed ← 10^-6 [MPa]
        else
            F^{i+1} ← F^i + kΔF
            i ← i + 1
        end if
    else
        Convergence ← False
    end if
end while
```

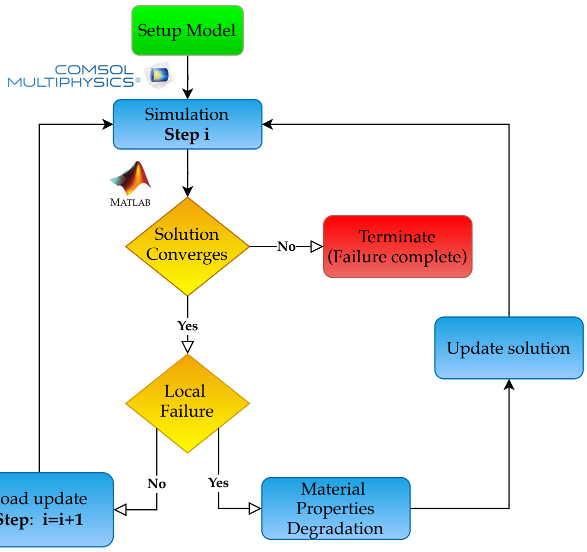

Fig. 6. Iterative numerical procedure implemented to simulate fracture in the FE vertebral models.

We used a quasi-static force-driven incremental approach to simulate the local progressive damage of the bone within the overall vertebra domain. The total applied force at load step $i+1$, i.e. F^{i+1}, was updated by following the iterative rule:

$$F^{i+1} = F^i + k\Delta F \tag{3}$$

where F^i is the total applied force at the previous load step, $\Delta F = 100\,\mathrm{N}$ a constant load increment, and k a load rate defined inversely proportional to the ratio of fractured element with respect to the total number of finite elements. The chosen strategy allows us to adaptively increment the load application rate entailing an effective and complete analysis of bone fractures reducing, at the same time, the computational effort. At each incremental step, the solution is computed, and the stress and strain fields and the vertebral reaction force are evaluated. The latter was quantified as the surface integral of the three components of the reaction forces on the L4 top endplate. By using the failure criteria described in Section 2.3.1, the local onset of damage was checked. Once the failure was locally detected, we updated material properties according to the degradation law described in Section 2.3.1. In particular, within the current load step, keeping fixed the geometry model and boundary conditions, the iterative process was repeated until no further bone failure occurred. Otherwise, if the failure criterion was not satisfied, the computational model was updated to the next step by increasing the applied load. Finally, we assumed a completely failed vertebra when the numerical solution no longer converged. Accordingly, we identified the ultimate compressive force, R_u, as the maximum load recorded before an abrupt increase in the top endplate displacement, i.e. non-converged solution.

3. Results

3.1. Convergence Analysis

Convergence analysis was performed using the uninstrumented L4 model and adopting an h-refinement approach for the finite element (FE) discretization [21, 33]. We tested 11 different meshes considering a maximum element size $d_\mathrm{max} \in 1.5 \div 6\,\mathrm{mm}$. As previously mentioned (Section 2.1), we set the minimum element size as $d_\mathrm{min} = d_\mathrm{max}/2$ to make the finite element discretization as uniform as possible. We provide the complete description of mesh parameters for the different models in Table. 2.

Table 2
Mesh refinement models (Mod 1-11) adopted for convergence analysis. We provide maximum (d_max), minimum (d_min) and average (d_avg) element size expressed in [mm], along with the number of tetrahedral elements (NoE). We assume model 11 as reference solution for error evaluation.

	Mod 1	**Mod 2**	**Mod 3**	**Mod 4**	**Mod 5**	**Mod 6**	**Mod 7**	**Mod 8**	**Mod 9**	**Mod 10**	**Mod 11**
d_{max}	6.00	4.00	3.50	3.00	2.50	2.20	2.00	1.90	1.80	1.70	1.60
d_{min}	3.00	2.00	1.75	1.50	1.25	1.10	1.00	0.95	0.90	0.85	0.80
d_{avg}	5.06	3.45	3.04	2.61	2.17	1.91	1.73	1.65	1.56	1.47	1.40
NoE	11120	27739	39884	62688	107240	158728	212089	248728	291875	346857	416157

We compare numerical solutions from the different meshes by tacking the finest FE discretization model (i.e. Mod 11) as the reference solution, and compute the error for each model in terms of: *i)* reaction force R at the second load step, *ii)* mean von Mises stress $\overline{\sigma}_{vm}$, and *iii)* total strain energy W_s. As commonly accepted [29], we assume a converged mesh for an error threshold of 5%. Accordingly, we provide the behavior of the three error parameters with respect to the total number of tetrahedral elements (NoE) in Fig. 7(a) and to the mean element size d_avg in Fig. 7(b), for each model tested under flexion loading. The analysis highlighted that model 7 fulfils the error estimate bound. Accordingly, the chosen computational model for the L4 vertebra used in the following analysis will consist of $d_\mathrm{min} = 1\,\mathrm{mm}$, $d_\mathrm{max} = 2\,\mathrm{mm}$, thus resulting in a total of 212089 tetrahedral elements and 882505 degrees of freedom.
Screws were meshed with minimum and maximum elements size of 0.1 mm and 1 mm, respectively. It is worth noticing that the actual number of elements in the instrumented models varied according to the

different implant configurations (i.e. angles). Specifically, FE discretizations ranged between 223172 ± 5475 elements for the vertebra and 61991 ± 130 for the screws domains.

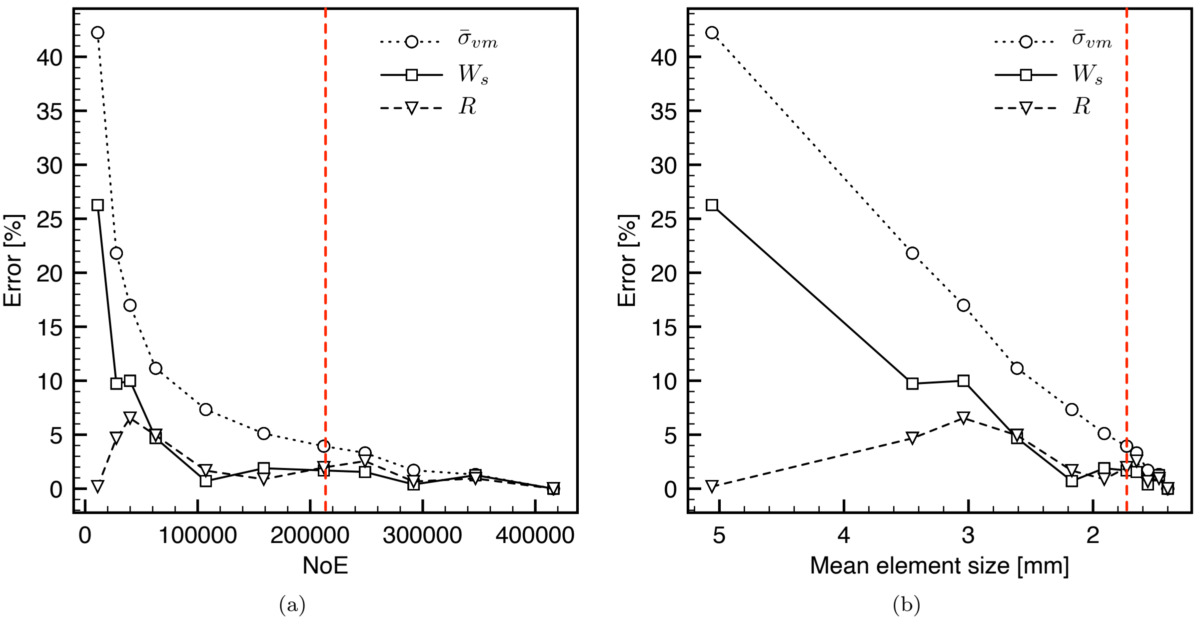

Fig. 7. Convergence analysis for the uninstrumented L4 model under flexion. Error behavior for reaction force, R, at the top L4 endplate (selected at the second loading step), mean von Mises stress, $\overline{\sigma}_{vm}$, and total strain energy, W_s, versus (a) number of elements (NoE), and (b) average element size (d_{avg}). The vertical lines identify model 7, viz, the one resulting from the convergence analysis.

3.2. Data preprocessing, statistical analysis and model validation

Data extraction. We conducted a total of 54 fracture analyses, resulting from 6 test loading modes differentiated among 9 screw configuration angles. For the sake of notation, we will refer to screws combinations as (CC, ML) indicating craniocaudal and mediolateral angles, respectively. The overall computational time required was about 8 days, on an HP Z640 workstation with E5-2630 v3 (8 × 2.40 GHz) and 32 GB of RAM. Because each fracture analysis included a different number of load steps and a large amount of data, a pre-processing phase was needed. Within a generic loading step, stresses ($\sigma_{vm}, \sigma_{max}, \sigma_{min}$) and strains ($\epsilon_{max}, \epsilon_{min}$) were evaluated at each node of the bony domain. A median filter was applied (box size 5), to remove fictitious values that can be derived from local material property discontinuities as introduced by the degradation rule in Section 2.3.1. Maximum and average values were computed, along with the reaction force on the top endplate R and the fracture volume $\mathrm{V_f}$ (volume integral on the failed bony domain). To select a single representative measurement within the entire sequence of loading steps, we chose the maximum value for each variable. We obtained, therefore, 13 field variables including the ultimate compressive force, R_{u}, representing the complete dataset used in the statistical analyses. In the following we will refer to the maximum values fo stresses and strains as $\widehat{\sigma}$, $\widehat{\epsilon}$, while to the mean values as $\bar{\sigma}$, $\bar{\epsilon}$.

Statistical analyses. We used descriptive statistics to investigate the influence of screw insertion angles and loading modes on the biomechanics of L4 vertebra. Loading modes and screws combinations were assumed as independent field variables alternatively, to perform two separate statistical analyses, i.e. one-way analysis of variance (ANOVA) and multivariate analysis of variance (MANOVA). ANOVA was performed on each field variable examining pairwise differences via a Tukey-Kramer post-hoc test. Homogeneity of variance assumption was ensured for all 13 descriptors by using Levene's F test. Homoscedasticity was satisfied for 12 field variables suggesting the appropriateness of ANOVA in the present case. The only heteroscedastic variable not meeting the ANOVA's assumptions was R_u when grouping data by loading modes. To overcome this problem, we used the Kruskal-Wallis nonparametric test in place of ANOVA for R_u. MANOVA was further used considering maximum values of stresses $(\widehat{\sigma}_{vm}, \widehat{\sigma}_{max}, \widehat{\sigma}_{min})$ as dependent variables. A series of Pearson correlations were performed to ensure MANOVA's assumption regarding the correlation between dependent variables. This hypothesis was confirmed and multicollinearity was excluded since, as suggested by Tabachnick and Fidell [53], no correlation should result above $\rho = 0.90$. Ultimately, univariate ANOVAs were employed as post-hoc tests.

Model validation. Models showed an ultimate force of 4269 ± 1114 N which is in good agreement with available experimental results [9, 10, 47, 48, 49, 50, 54]. Such a result allows us to consider our model validated according to Jones at al. [29], since the most commonly reported form of direct validation in single vertebral models consists in the comparison of predicted vertebral force with in vitro experimental results.

3.3. Fracture pattern

Among the variability of fracture patterns observed within the 54 configurations, we identified two main distinct behaviours: (1) brittle-like (83%) and (2) ductile-like (17%) fracture. A brittle-like fracture is characterised by a negligible plastic deformation before failure, thus presenting a quasi-constant stiffness. Conversely, a ductile-like fracture shows a sizeable plastic deformation region before failure, dramatically reducing the overall structural stiffness. Figure 8 shows the load-displacement curves for two selected cases (CC, ML), namely (0,+5) and (-5,-5), when loaded in flexion. As expected, brittle fracture occurs within 0.07 mm displacement and involves up to 3600 N loading force. Ductile fracture, instead, appears after 0.33 mm displacement (i.e. five times larger) and involves around 3000 N of loading force.

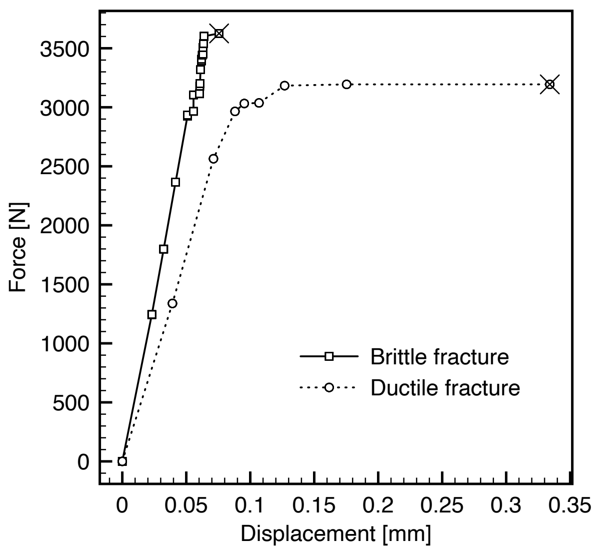

Fig. 8. Load-displacement curves for the two observed fracture patterns: brittle fracture (solid), ductile fracture (dashed).

The ductile fracture occurred when the fracture evolved in the posteroanterior direction, involving the whole vertebral body, as shown in Fig.1. Due to the large part of trabecular bone in the vertebra body, failure patterns are different than the one observed in long bones, e.g. the femur [21, 22]. Vertebra can show plastic-like behaviour undergoing large deformations before fracture.

On the contrary, brittle fracture occurred when the applied boundary condition induced a stress concentration in the pedicular region, consisting of cortical bone mainly. A symmetrical brittle fracture (see Fig. 9(a)) was observed in the case of extension and flexion, while LAR, RAR, LLB, and RLB were associated with an asymmetrical fracture pattern (see Fig. 9(b)), rapidly evolving in the most solicited side.

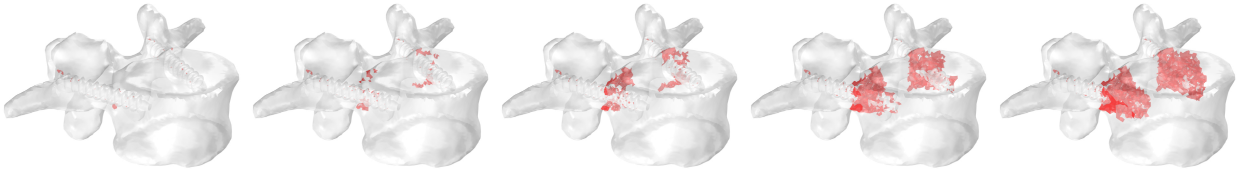

(a) Brittle fracture with symmetrical pattern: Flexion, Extension.

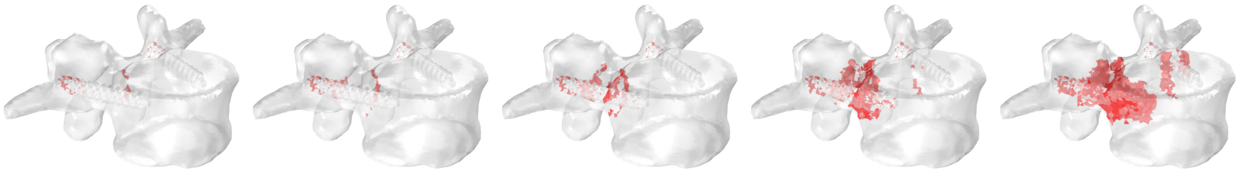

(b) Brittle fracture with asymmetrical pattern: LAR, RAR, LLB, RLB.

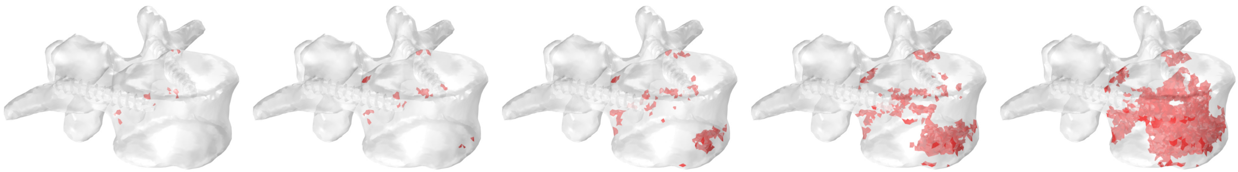

(c) Ductile fracture: combination (CC, ML) = $(-5,-5)$ in every loading mode, (0,-5) and (-5,0) in Extension, (+5,0) in RAR.

Fig. 9. Comparison of recurrent fracture patterns occurring among the overall computational analysis. (a) Brittle fracture occurring when the pedicular region is concerned. (b) Brittle asymmetrical fracture obtained when screws are not loaded symmetrically. (c) Ductile fracture involving the whole vertebral body.

Few exceptions (see Table 3) suggest that also the placement of the screws may influence the fracture pattern. In particular, the case (-5,+5) showed a right asymmetrical fracture pattern while a symmetric one was expected under flexion. On the contrary, a symmetric fracture pattern was found for combinations in which a right (LLB, RAR) or left (LAR, RLB) asymmetrical failure was expected.

Table 3
Tested combinations with atypical fracture patterns concerning loading mode: flexion (F), extension (E), left (counterclockwise) and right (clockwise) axial rotation (LAR, RAR), left and right lateral bending (LLB, RLB).

Loading Mode	**Combination (CC, ML)**	**Fracture type**
F	(-5,+5)	Right asymmetrical
LLB	(0,+5)	Symmetrical
	(-5,+5)	Symmetrical
RLB	(-5,+5)	Symmetrical
	(-5,-5)	Symmetrical
LAR	(-5,+5)	Symmetrical
RAR	(+5,0) (-5,-5)	Symmetrical Symmetrical

3.4. Screws combination comparison

Figure 10 provides an overview of 9 descriptors (max and average stresses, $\widehat{\sigma}$, $\bar{\sigma}$, reaction force, R, fracture volume, V_f and ultimate force, R_u) varying mediolateral and craniocaudal angles. For each combination (CC,ML) we mediated the dataset over the six loading modes, such to get comparable quantities. Observables are arranged according to a risk color code mapping, i.e.: high values of stresses (red) correspond to low values of fracture volume, reaction force and ultimate force.

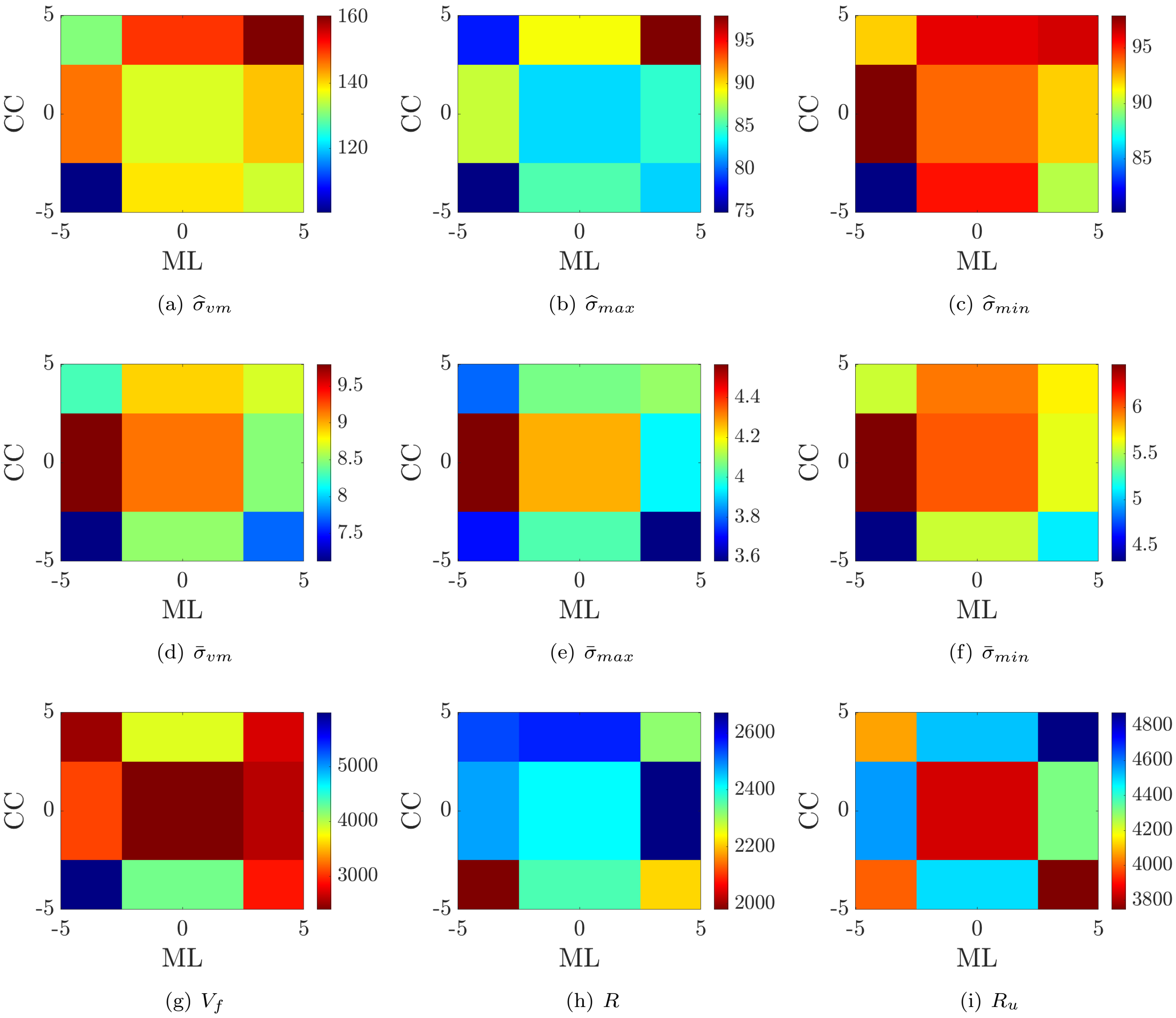

(a) $\widehat{\sigma}_{vm}$ (b) $\widehat{\sigma}_{max}$ (c) $\widehat{\sigma}_{min}$

(d) $\bar{\sigma}_{vm}$ (e) $\bar{\sigma}_{max}$ (f) $\bar{\sigma}_{min}$

(g) V_f (h) R (i) R_u

Fig. 10. Comparison between screws insertion angle combinations. Data for each combination are obtained averaging the results for the six loading modes.

Overall, combination (CC, ML) $= (-5, -5)$ exhibits very low stresses (both average and maximum) together with a reduced ultimate force and reaction force while highlighting the highest value of the fracture volume. Given the reduced level of stresses, this reflects the fact that such a configuration allows a greater propagation of the fracture before the complete vertebral failure occurs (ductile fracture). Similar reasoning leads to the conclusion that $(+5, +5)$ and $(0, -5)$ might be the most critical cases. The first shows the largest maximum stresses, ultimate force, and low fracture volume, while the second stands out for greater average stresses. We found quantitative statistical agreement through MANOVA and ANOVA tests shown in Tables A.4 and

A.5, respectively. In particular, we found statistically significant differences between screws combinations based on multivariate analyses. The univariate tests led to significant results for $\widehat{\sigma}_{vm}$, $\widehat{\sigma}_{min}$, $\widehat{\epsilon}_{min}$ and $\bar{\sigma}_{min}$. Follow-up tests indicated case $(-5, -5)$ as the least critical. Besides, we found non-significant differences amongst the remaining combinations.

3.5. Loading modes comparison

A similar approach presented in the previous section was used to investigate the influence of the loading modes on the biomechanical outcome of the vertebra. Figure 11 compares the response of the model for the loading modes in terms of cumulative results (sum for each variable from all nine screws trajectories). We observe the absence of a radically counter-trend loading mode. As regards maximum stresses, Fig.s 11(a)–11(c) show small fluctuations around the average ($\leq 8\,\%$) with slightly higher values of $\widehat{\sigma}_{vm}$ and $\widehat{\sigma}_{min}$ in right lateral bending and $\widehat{\sigma}_{max}$ in extension. A similar picture emerges in terms of reaction force, see Fig. 11(h), together with an increased variability ($\leq 19\,\%$). Figures 11(d)–11(f) reveal larger variations for the cumulative mean stresses ($\leq 15\,\%$) showing highest values in extension and left axial rotation. Fracture volume in Fig. 11(g) shows the highest variability among the 9 descriptors in right axial rotation mode, clearly outstanding in the other cases with a cumulative fracture volume $40\,\%$ higher than the average. A similar trend is observed for the ultimate compressive force in Fig. 11(i).

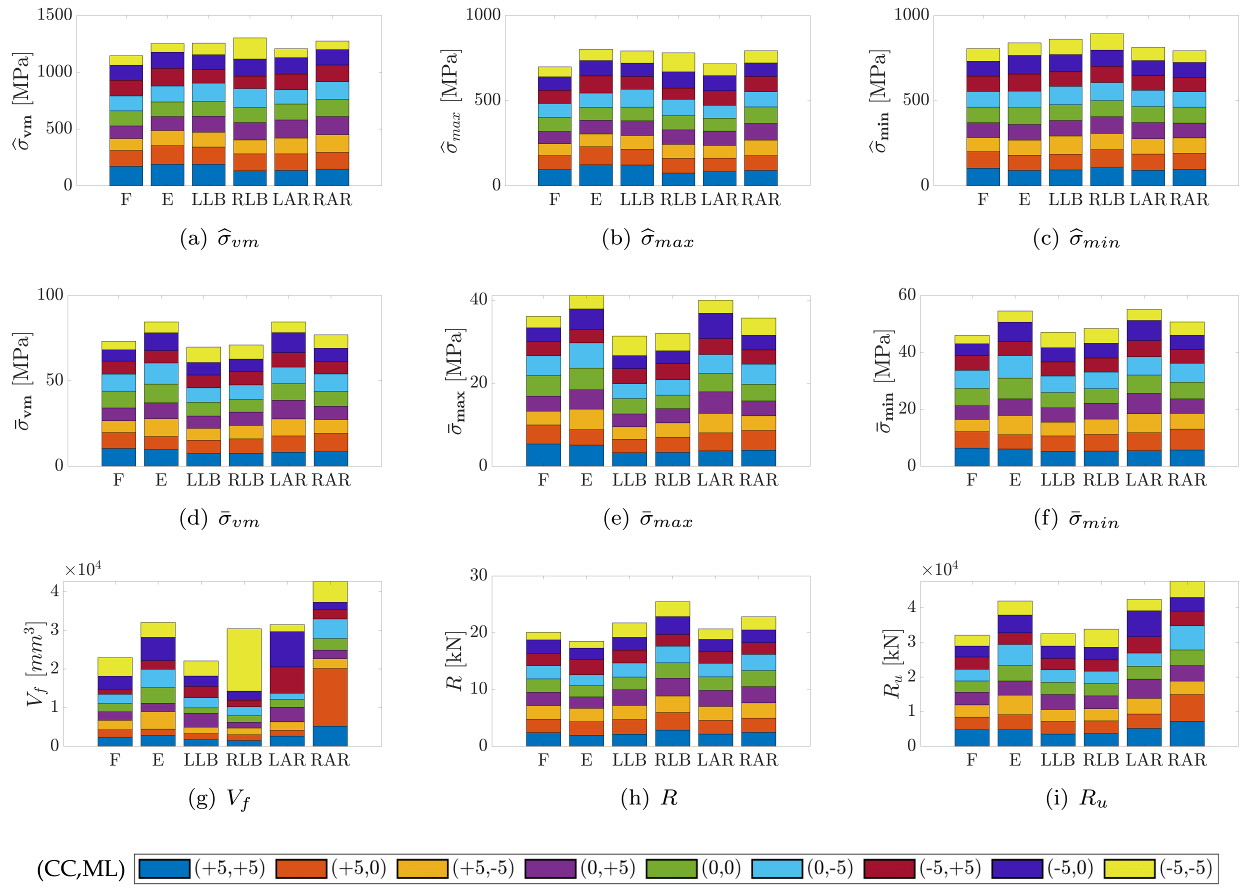

Fig. 11. Comparison between loading modes: flexion (F), extension (E), left (counterclockwise) and right (clockwise) axial rotation (LAR, RAR), left and right lateral bending (LLB, RLB). Data for each loading mode are obtained as the sum of results for all nine screws combinations.

Tables B.6 and B.7 present the statistical quantitative comparison in terms of loading modes resulting for

MANOVA and ANOVA tests, respectively. In particular, the multivariate analysis resulted in statistically significant differences between loading modes. Accordingly, the univariate tests indicated significant results for R, R_u, $\widehat{\sigma}_{min}$ and $\bar{\epsilon}_{max}$, $\bar{\epsilon}_{min}$, $\bar{\sigma}_{max}$, $\bar{\sigma}_{vm}$. Follow-up tests performed on the reaction force, the maximum σ_{min}, and the mean σ_{vm}, indicated the right lateral bending as the most critical loading mode. However, the same tests performed on R_u, $\bar{\epsilon}_{max}$, $\bar{\epsilon}_{min}$, and $\bar{\sigma}_{max}$ did not support this assumption. Based on such results, no strong evidence was found to highlight any of the loading modes as the most, nor the least critical.

4. Discussion

This study has been carried on with two goals: (i) to understand the importance of pedicle screw angles in fracture occurrence for physiological loads acting on instrumented vertebra models; (ii) to identify the mechanical field components allowing for a clinical translation based on robust statistical analyses. Thus the study focuses on the structural aspects of the bone material distribution and on the mechanical conditions that compromise the stability of the device, and do not tackle the actual cues (biological, chemical, and physiopathological) that trigger fracture in the bone. Numerical results and statistical analyses indicate that among the several screws insertion trajectories, the caudomedial one, i.e. (-5,-5) is the safest in preventing vertebral fractures, maybe because such screw direction maximises the area of the bone-screw interface. Spine surgeons could take advantage of current data when inserting screws at the lumbar vertebrae during spinal fusion procedures.

We propose a simplified constitutive model enforcing a patient-specific heterogeneous distribution of materials parameters within an accurate geometry model of L4 vertebra, bilaterally instrumented with pedicle screws. We considered a clinical CT scan to build up a patient-specific FE model because of possible clinical use [14, 35, 55, 56]. Nine screws trajectories were defined and tested in multiaxial loading (mimicking physiological motion and following clinical guidelines) up to fracture since no clear statistical indication on the most critical loading mode is known.

The analysis of stress distribution and peak/average stress levels are thought to be relevant for fracture risk assessment [57, 58, 59]. Accordingly, we assumed that screw angulation (both craniocaudal and mediolateral) affects the biomechanical response of the instrumented vertebra. In this perspective, based on statistical inference, we observed that the caudomedial trajectory, i.e $(-5, -5)$, resulted in the least critical case. Contrariwise, medial $(0, -5)$ or craniolateral $(+5, +5)$ trajectories led to higher stresses (both peak and average) without a clear statistical significance. Based on our extended analysis and in agreement with data reported in Newcomb et al. [14] for the cortical bone, we concluded that a medial and caudal trajectory, i.e. $(-5, -5)$, may be safer from a clinical point of view. However, for the critical cases, we also observed higher values for the reaction force R and ultimate force R_u, which may indicate increased fracture strength. This finding, together with the high-stress levels, may be explained by an increased engagement of the screws with the cortical bone. Trajectories involving a more medio-to-lateral path, i.e cortical bone trajectory, are based on this assumption and have been demonstrated to show increased stability of the bone-screw interface [7, 13].

Future studies require to investigate the anchorage performance of the different trajectories assessing the pullout strength (POS) as reported in numerous studies involving spinal implants [11, 13, 60]. In our opinion, high levels of stress remain a critical factor independently on the fixation strength, since it may be detrimental to the structural integrity of the bone increasing the risk of failure and screw loosening in the long term.

Limitations. There are some limitations to this study that should be mentioned. First, boundary conditions for extended spine models [35] are difficult to apply to the present study since we considered a single vertebral model. There are no studies, to date, documenting how to replicate the physiological movement at the single spine level. Second, the current study focused on a single patient-specific model, and a wider clinical cohort would be necessary to support and validate the proposed findings. Third, different screw insertion points and screw design could affect the results in a non-negligible way. Further, bone was assumed as a linear elastic isotropic material and more complex material models should be introduced to further generalise the present computational framework. In particular, multiscale homogenised constitutive descriptions are foreseen embedding a physiological description of the multi-phase material components in view of remodelling processes [61, 62, 63, 64]. Lastly, advanced FE descriptions, machine learning and imaging techniques, and improved numerical convergence will be required to integrate complex patient-specific geometry models with advanced constitutive laws [65, 66, 67, 68].

Future perspectives. We conclude by pointing out potential future developments of the present model that we aim to accomplish in forthcoming contributions. As mentioned, a specific analysis of pullout strength could enrich the clinical evaluation of the vertebra-screw construct. Modelling larger regions of the spine (for example FSU [69] and its extensions [70]), including intervertebral discs and surrounding soft tissues (e.g ligaments, muscles), would allow for a more robust computational analysis. Furthermore, the introduction of a nonlinear poroelastic constitutive model for the trabecular bone could match elastoplastic [46], anisotropic [71] and compressible [21, 22] phenomena expected to occur in the human bone.

Acknowledgment

AG and CF are grateful to the Italian GNFM-INdAM for partial supporting this work.

References

[1] E. Rutherford, L. Tarplett, E. Davies, J. Harley, L. King, Lumbar spine fusion and stabilization: Hardware, techniques, and imaging appearances1, Radiographics : a review publication of the Radiological Society of North America, Inc 27 (2007) 1737–1749. doi:10.1148/rg.276065205.

[2] G. Vadalà, A. Di Martino, F. Russo, M. Tirindelli, L. Felice, F. Agostini, R. Papalia, V. Denaro, Autologous bone marrow concentrate combined with platelet-rich plasma enhance bone allograft potential to induce spinal fusion, Journal of biological regulators and homeostatic agents 30 (2016) 173–180.

[3] A. Momin, M. Steinmetz, The evolution of minimally invasive lumbar spine surgery, World Neurosurgery In Press. doi:10.1016/j.wneu.2020.05.071.

[4] H. Defino, H. Costa, A. Nunes, M. Nogueira-Barbosa, V. Romero, Open versus minimally invasive percutaneous surgery for surgical treatment of thoracolumbar spine fractures- a multicenter randomized controlled trial: study protocol, BMC Musculoskeletal Disorders 20 (2019) 397. doi:10.1186/s12891-019-2763-1.

[5] J. Hicks, A. Singla, F. Shen, V. Arlet, Complications of pedicle screw fixation in scoliosis surgery a systematic review, Spine 35 (2010) E465–470. doi:10.1097/BRS.0b013e3181d1021a.

[6] F. Galbusera, D. Volkheimer, S. Reitmaier, N. Berger-Roscher, A. Kienle, H.-J. Wilke, Pedicle screw loosening: a clinically relevant complication?, European Spine Journal 24 (2015) 1005–1016. doi:10.1007/s00586-015-3768-6.

[7] B. Santoni, R. Hynes, K. Mcgilvray, G. Rodriguez-Canessa, A. Lyons, M. Henson, W. Womack, C. Puttlitz, Cortical bone trajectory for lumbar pedicle screws, The Spine Journal 9 (2008) 366–373. doi:10.1016/j.spinee.2008.07.008.

[8] M. Hussain, R. Natarajan, A. Fayyazi, B. Braaksma, G. Andersson, H. An, Screw angulation affects bone-screw stresses and bone graft load sharing in anterior cervical corpectomy fusion with a rigid screw-plate construct: a finite element model study, The Spine Journal 9 (2009) 1016–1023. doi:10.1016/j.spinee.2009.08.461.

[9] H. Giambini, X. Qin, D. Dragomir-Daescu, K.-N. An, A. Nassr, Specimen-specific vertebral fracture modeling: A feasibility study using the extended finite element method, Medical & Biological Engineering & Computing 54 (2015) 583–593. doi:10.1007/s11517-015-1348-x.

[10] M. Mirzaei, A. Zeinali, A. Razmjoo, M. Nazemi, On prediction of the strength levels and failure patterns of human vertebrae using quantitative computed tomography (qct)-based finite element method, Journal of Biomechanics 42 (2009) 1584–1591. doi:10.1016/j.jbiomech.2009.04.042.

[11] J. Biswas, T. Sahu, M. Rana, S. Roy, S. Karmakar, S. Majumder, A. Roychowdhury, Design factors of lumbar pedicle screws under bending load: A finite element analysis, Biocybernetics and Biomedical Engineering 39 (2019) 52–62. doi:10.1016/j.bbe.2018.10.003.

[12] S.-I. Chen, R.-M. Lin, C.-H. Chang, Biomechanical investigation of pedicle screw-vertebrae complex: A finite element approach using bonded and contact interface conditions, Medical Engineering & Physics 25 (2003) 275–282. doi:10.1016/S1350-4533(02)00219-9.

[13] K. Matsukawa, Y. Yato, H. Imabayashi, N. Hosogane, T. Asazuma, K. Nemoto, Biomechanical evaluation of the fixation strength of lumbar pedicle screws using cortical bone trajectory: A finite element study, Journal of Neurosurgery: Spine 23 (2015) 1–8. doi:10.3171/2015.1.SPINE141103.

[14] A. Sawa, S. Baek, B. Kelly, N. Crawford, Effect of screw position on load transfer in lumbar pedicle screws: a non-idealized finite element analysis, Computer Methods in Biomechanics and Biomedical Engineering 20 (2016) 1–11. doi:10.1080/10255842.2016.1209187.

[15] J. Li, J. Shang, Y. Zhou, C. Li, H. Liu, Finite element analysis of a new pedicle screw-plate system for minimally invasive transforaminal lumbar interbody fusion, PloS One 10 (2015) e0144637. doi:10.1371/journal.pone.0144637.

[16] C. Liu, A. Kamara, Y. Yan, Investigation into the biomechanics of lumbar spine micro-dynamic pedicle screw, BMC Musculoskeletal Disorders 19 (231). doi:10.1186/s12891-018-2132-5.
[17] Z. Yosibash, R. Padan, L. Joskowicz, C. Milgrom, A ct-based high-order finite element analysis of the human proximal femur compared to in-vitro experiments, Journal of biomechanical engineering 129 (2007) 297–309. doi:10.1115/1.2720906.
[18] A. Jones, R. Wilcox, Assessment of factors influencing finite element vertebral model predictions, Journal of biomechanical engineering 129 (2008) 898–903. doi:10.1115/1.2800791.
[19] A. Vesterby, L. Mosekilde, H. Gundersen, F. Melsen, L. Mosekilde, K. Holme, S. Sørensen, Biologically meaningful determinants of the in vitro strength of lumbar vertebrae, Bone 12 (3) (1991) 219–224. doi:https://doi.org/10.1016/8756-3282(91)90044-J.
[20] M. Silva, C. Wang, T. Keaveny, W. Hayes, Direct and computed tomography thickness measurements of the human, lumbar vertebral shell and endplate, Bone 15 (1994) 409–414. doi:10.1016/8756-3282(94)90817-6.
[21] C. Falcinelli, A. Martino, A. Gizzi, G. Vairo, V. Denaro, Mechanical behavior of metastatic femurs through patient-specific computational models accounting for bone-metastasis interaction, Journal of the Mechanical Behavior of Biomedical Materials 93 (2019) 9–22. doi:10.1016/j.jmbbm.2019.01.014.
[22] C. Falcinelli, A. Martino, A. Gizzi, G. Vairo, V. Denaro, Fracture risk assessment in metastatic femurs: a patient-specific ct-based finite-element approach, Meccanica 55 (2019) 861–881. doi:10.1007/s11012-019-01097-x.
[23] A. Sternheim, O. Giladi, Y. Gortzak, M. Drexler, M. Salai, N. Trabelsi, C. Milgrom, Z. Yosibash, Pathological fracture risk assessment in patients with femoral metastases using ct-based finite element methods. a retrospective clinical study, Bone 110 (2018) 215–220. doi:https://doi.org/10.1016/j.bone.2018.02.011.
[24] S. C. Cowin, Bone Mechanics, Vol. 9, Taylor & Francis, 1981. arXiv:https://doi.org/10.3109/10731198109119616, doi:10.3109/10731198109119616.
[25] Z. Yosibash, N. Trabelsi, C. Milgrom, Reliable simulations of the human proximal femur by high-order finite element analysis validated by experimental observations, Journal of Biomechanics 40 (16) (2007) 3688–3699. doi:https://doi.org/10.1016/j.jbiomech.2007.06.017.
[26] E. Morgan, T. Keaveny, Trabecular bone modulus-density relationships depend on anatomic site, Journal of Biomechanics 36 (2003) 897–904. doi:10.1016/S0021-9290(03)00071-X.
[27] E. Morgan, T. Keaveny, Dependence of yield strain of human trabecular bone on anatomic site, Journal of Biomechanics 34 (2001) 569–577. doi:10.1016/S0021-9290(01)00011-2.
[28] H. H. Bayraktar, E. F. Morgan, G. L. Niebur, G. E. Morris, E. K. Wong, T. M. Keaveny, Comparison of the elastic and yield properties of human femoral trabecular and cortical bone tissue, Journal of Biomechanics 37 (1) (2004) 27–35. doi:https://doi.org/10.1016/S0021-9290(03)00257-4.
[29] A. Jones, R. Wilcox, Finite element analysis of the spine: Towards a framework of verification, validation and sensitivity analysis, Medical Engineering & Physics 30 (2009) 1287–1304. doi:10.1016/j.medengphy.2008.09.006.
[30] T. Keaveny, E. Morgan, G. Niebur, O. Yeh, Biomechanics of trabecular bone, Annual Review of Biomedical Engineering 3 (2001) 307–333. doi:10.1146/annurev.bioeng.3.1.307.
[31] J. Keyak, I. Lee, H. Skinner, Correlations between orthogonal mechanical properties and density of trabecular bone: Use of different densitometric measures, Journal of Biomedical Materials Research 28 (1994) 1329–1336. doi:10.1002/jbm.820281111.
[32] T. S. Keller, Predicting the compressive mechanical behavior of bone, Journal of Biomechanics 27 (9) (1994) 1159–1168. doi:https://doi.org/10.1016/0021-9290(94)90056-6.
[33] C. Falcinelli, E. Schileo, L. Balistreri, F. Baruffaldi, B. Bordini, M. Viceconti, U. Albisinni, F. Ceccarelli, L. Milandri, A. Toni, F. Taddei, Multiple loading conditions analysis can improve the association between finite element bone strength estimates and proximal femur fractures: A preliminary study in elderly women, Bone 67 (2014) 71–80. doi:https://doi.org/10.1016/j.bone.2014.06.038.
[34] Z. Yosibash, D. Tal, N. Trabelsi, Predicting the yield of the proximal femur using high-order finite-element analysis with inhomogeneous orthotropic material properties, Phil. Trans. R. Soc. A. 368 (1920) (2010) 2707–2723. doi:10.1098/rsta.2010.0074.
[35] M. Dreischarf, T. Zander, A. Shirazi-Adl, C. Puttlitz, C. Adam, C.-S. Chen, V. Goel, A. Kiapour, Y. Kim, K. Labus, J. Little, W. M. Park, Y. Wang, H. Wilke, A. Rohlmann, H. Schmidt, Comparison of eight published static finite element models of the intact lumbar spine: Predictive power of models improves when combined together, Journal of Biomechanics 47 (2014) 1757–1766. doi:10.1016/j.jbiomech.2014.04.002.
[36] S. Kushchayev, T. Glushko, M. Jarraya, K. Schuleri, M. Preul, M. Brooks, O. Teytelboym, Abcs of the degenerative spine, Insights into Imaging 9 (2018) 253–274. doi:10.1007/s13244-017-0584-z.
[37] S. Garfin, F. J. Eismont, G. R. Bell, C. Bono, M. J. Fischgrund, Rothman-Simeone and Herkowitz's The Spine, 2 Vol Set, 7th Edition, Elsevier, Philadelphia, PA, 2017.
[38] C.-K. Chao, C.-C. Hsu, J.-L. Wang, J. Lin, Increasing bending strength and pullout strength in conical pedicle screws: Biomechanical tests and finite element analyses, Journal of Spinal Disorders & Techniques 21 (2008) 130–138. doi:10.1097/BSD.0b013e318073cc4b.
[39] M. Xu, J. Yang, I. Lieberman, R. Haddas, Stress distribution in vertebral bone and pedicle screw and screw–bone load transfers among various fixation methods for lumbar spine surgical alignment: A finite element study, Medical Engineering & Physics 63 (2018) 26–32. doi:10.1016/j.medengphy.2018.10.003.
[40] K. Li, C. Wang, J. Yan, Q. Zhang, B. Dang, Z. Wang, Y. Yao, K. Lin, Z. Guo, L. Bi, Y. Han, Evaluation of the osteogenesis and osseointegration of titanium alloys coated with graphene: An in vivo study, Scientific Reports 8 (1843). doi:10.1038/s41598-018-19742-y.

[41] C. Giordano, E. Sandrini, B. Del Curto, E. Signorelli, G. Rondelli, L. Di Silvio, Comparison between a novel biomimetic treatment and commercially exploited surfaces, Journal of Applied Biomaterials & Biomechanics 2 (2004) 35–44.
[42] L. Lin, H. Wang, M. Ni, Y. Rui, T.-Y. Cheng, C.-K. Cheng, X. Pan, G. Li, C. Lin, Enhanced osteointegration of medical titanium implant with surface modifications in micro/nanoscale structures, Journal of Orthopaedic Translation 2 (1) (2014) 35–42. doi:https://doi.org/10.1016/j.jot.2013.08.001.
[43] E. Schileo, F. Taddei, L. Cristofolini, M. Viceconti, Subject-specific finite element models implementing a maximum principal strain criterion are able to estimate failure risk and fracture location on human femurs tested in vitro, Journal of Biomechanics 41 (2008) 356–367. doi:10.1016/j.jbiomech.2007.09.009.
[44] K. Bozic, J. Keyak, H. Skinner, H. Bueff, D. Bradford, Three-dimensional finite element modeling of a cervical vertebra, Journal of Spinal Disorders 7 (1994) 102–110. doi:10.1097/00002517-199407020-00002.
[45] Y. Matsuura, H. Giambini, Y. Ogawa, Z. Fang, A. Thoreson, M. Yaszemski, L. Lu, K.-N. An, Specimen-specific nonlinear finite element modeling to predict vertebrae fracture loads after vertebroplasty, Spine 39 (2014) E1291–E1296. doi:10.1097/BRS.0000000000000540.
[46] K. Imai, I. Ohnishi, M. Bessho, K. Nakamura, Nonlinear finite element model predicts vertebral bone strength and fracture site, Spine 31 (2006) 1789–1794. doi:10.1097/01.brs.0000225993.57349.df.
[47] A. Bruno, K. Burkhart, B. Allaire, D. Anderson, M. Bouxsein, Spinal loading patterns from biomechanical modeling explain the high incidence of vertebral fractures in the thoracolumbar region, Journal of Bone and Mineral Research 32 (2017) 1282–1290. doi:10.1002/jbmr.3113.
[48] J. Choisne, J.-M. Valiadis, C. Travert, S. Kolta, C. Roux, W. Skalli, Vertebral strength prediction from bi-planar dual energy x-ray absorptiometry under anterior compressive force using a finite element model: an in vitro study, Journal of the Mechanical Behavior of Biomedical Materials 87 (2018) 190–196. doi:10.1016/j.jmbbm.2018.07.026.
[49] W. Curry, F. Pintar, N. Doan, H. Nguyen, G. Eckardt, J. Baisden, D. Maiman, G. Paskoff, B. Shender, B. Stemper, Lumbar spine endplate fractures: Biomechanical evaluation and clinical considerations through experimental induction of injury, Journal of Orthopaedic Research 34 (2015) 1084–1091. doi:10.1002/jor.23112.
[50] A. Rezaei, H. Giambini, K. Carlson, H. Xu, S. Uthamaraj, D. Dragomir-Daescu, M. Yaszemski, L. Lu, Mechanical testing setups affect spine segment fracture outcomes, Journal of the Mechanical Behavior of Biomedical Materials 100 (2019) 103399. doi:10.1016/j.jmbbm.2019.103399.
[51] Z. Sadiq, Bilateral pedicle stress fracture in the lumbar spine of a sedentary office worker, European Spine Journal 15 Suppl 5 (2006) 653–655. doi:10.1007/s00586-006-0184-y.
[52] S. Tarsuslugil, R. O'Hara, N. Dunne, F. Buchanan, J. Orr, D. Barton, R. Wilcox, Experimental and computational approach investigating burst fracture augmentation using pmma and calcium phosphate cements, Annals of Biomedical Engineering 42 (2014) 751–762. doi:10.1007/s10439-013-0959-3.
[53] B. Tabachnick, L. Fidell, J. Ullman, Using Multivariate Statistics, Pearson, 2018.
[54] C. Costa, P. Eltes, A. Lazáry, P. Varga, M. Viceconti, E. Dall'Ara, Biomechanical assessment of vertebrae with lytic metastases with subject-specific finite element models, Journal of the Mechanical Behavior of Biomedical Materials 98 (2019) 268–290. doi:10.1016/j.jmbbm.2019.06.027.
[55] G. Meijer, J. Homminga, A. Veldhuizen, G. Verkerke, Influence of interpersonal geometrical variation on spinal motion segment stiffness, Spine 36 (2011) E929–E935. doi:10.1097/BRS.0b013e3181fd7f7f.
[56] Y. Chevalier, P. Zysset, A patient-specific computer tomography-based finite element methodology to calculate the six dimensional stiffness matrix of human vertebral bodies, Journal of Biomechanical Engineering 134 (2012) 051006. doi:10.1115/1.4006688.
[57] A. Maknickas, V. Alekna, O. Ardatov, O. Chabarova, D. Zabulionis, M. Tamulaitiene, R. Kačianauskas, Fem-based compression fracture risk assessment in osteoporotic lumbar vertebra l1, Applied Sciences 9 (2019) 3013. doi:10.3390/app9153013.
[58] H. Takano, I. Yonezawa, M. Todo, H. Mazlan, T. Sato, K. Kaneko, Biomechanical study of vertebral compression fracture using finite element analysis, Journal of Applied Mathematics and Physics 05 (2017) 953–965. doi:10.4236/jamp.2017.54084.
[59] J. H. Keyak, S. A. Rossi, K. A. Jones, H. B. Skinner, Prediction of femoral fracture load using automated finite element modeling, Journal of Biomechanics 31 (2) (1997) 125–133. doi:https://doi.org/10.1016/S0021-9290(97)00123-1.
[60] K. Matsukawa, Y. Yato, H. Imabayashi, N. Hosogane, T. Asazuma, K. Nemoto, Biomechanical evaluation of cross trajectory technique for pedicle screw insertion: Combined use of traditional trajectory and cortical bone trajectory, Orthopaedic Surgery 7 (2015) 317–323. doi:10.1111/os.12212.
[61] G. Della Vecchia, m. l. de bellis, A. Pandolfi, A multiscale microstructural model of damage and permeability in fractured solids, Procedia Engineering 158 (2016) 21–26. doi:10.1016/j.proeng.2016.08.399.
[62] F. Concha, M. Sarabia-Vallejos, D. Hurtado, Micromechanical model of lung parenchyma hyperelasticity, Journal of the Mechanics and Physics of Solids 112 (2017) 126–144. doi:10.1016/j.jmps.2017.11.021.
[63] E. Monaldo, S. Brach, D. Kondo, G. Vairo, Effective mechanical response of non-linear heterogeneous materials comprising bimodular phases, European Journal of Mechanics - A/Solids 81 (2020) 103962. doi:10.1016/j.euromechsol.2020.103962.
[64] M. Soleimani, N. Muthyala, M. Marino, P. Wriggers, A novel stress-induced anisotropic growth model driven by nutrient diffusion: theory, fem implementation and applications in bio-mechanical problems, Journal of the Mechanics and Physics of Solids 144 (2020) 104097. doi:10.1016/j.jmps.2020.104097.
[65] D. Hurtado, N. Villarroel, J. Retamal, G. Bugedo, A. Bruhn, Improving the accuracy of registration-based biomechanical analysis: A finite element approach to lung regional strain quantification, IEEE Transactions on Medical Imaging 35 (2015) 580–588. doi:10.1109/TMI.2015.2483744.
[66] N. Barnafi, G. Gatica, D. Hurtado, Primal and mixed finite element methods for deformable image registration problems,

SIAM Journal on Imaging Sciences 11 (2018) 2529–2567. doi:10.1137/17M115219X.

[67] Y. Mei, D. Hurtado, S. Pant, A. Aggarwal, On improving the numerical convergence of highly nonlinear elasticity problems, Computer Methods in Applied Mechanics and Engineering 337 (2018) 110–127. doi:10.1016/j.cma.2018.03.033.

[68] M. Marino, P. Wriggers, Nearly-constrained transversely isotropic linear elasticity: energetically consistent anisotropic deformation modes for mixed finite element formulations, International Journal of Solids and Structures 202 (2020) 166–183. doi:10.1016/j.ijsolstr.2020.05.011.

[69] M. Stadelmann, G. Maquer, B. Voumard, A. Grant, D. Hackney, P. Vermathen, R. Alkalay, P. Zysset, Integrating mri-based geometry, composition and fiber architecture in a finite element model of the human intervertebral disc, Journal of the Mechanical Behavior of Biomedical Materials 85 (2018) 37–42. doi:10.1016/j.jmbbm.2018.05.005.

[70] R. Natarajan, K. Watanabe, K. Hasegawa, Posterior bone graft in lumbar spine surgery reduces the stress in the screw-rod system- a finite element study, Journal of the Mechanical Behavior of Biomedical Materials 104 (2020) 103628. doi:10.1016/j.jmbbm.2020.103628.

[71] G. U. Unnikrishnan, G. D. Barest, D. B. Berry, A. I. Hussein, E. F. Morgan, Effect of specimen-specific anisotropic material properties in quantitative computed tomography-based finite element analysis of the vertebra, Journal of Biomechanical Engineering 135 (10) (2013) 101007–101011. doi:10.1115/1.4025179.

Appendix A. Results of the statistical analyses for screws combinations comparison.

Table A.4
One-way MANOVA results for screws combinations comparison. Dependent variables employed were $\widehat{\sigma}_{vm}, \widehat{\sigma}_{max}, \widehat{\sigma}_{min}$.

Test Statistic	**Value**	$F^{(a)}$	$df_b{}^{(b)}$	$df_w{}^{(c)}$	**p-value**	**significance**$^{\mathbf{(d)}}$
Pillai's Trace	0.725	1.793	24	135	0.021	⋆
Wilks' Lambda	0.392	2.006	24	125	0.007	⋆
Hotelling's Trace	1.286	2.232	24	125	0.002	⋆
Roy's Largest Root	1.047 [e]	5.848	8	45	< 0.001	⋆

(a) F statistic: MS_b/MS_w.
(b) Degrees of freedom between groups.
(c) Degrees of freedom within groups.
(d) Significance level: $p < 0.05$.
(e) The statistic is an upper bound on F that yields a lower bound on the significance level.
∗ $(\bullet)_b$ and $(\bullet)_w$ denote *between* and *within* groups statistics.

Table A.5
One-way ANOVA results for screws combinations comparison.

Factor	$SS_b{}^{(a)}$	$df_b{}^{(b)}$	$df_w{}^{(c)}$	$MS_b{}^{(d)}$	$F^{(e)}$	**p-value**	**significance**$^{\mathbf{(f)}}$
$\widehat{\sigma}_{vm}$	1.32×10^4	8	45	1.66×10^3	3.73	0.002	⋆
$\widehat{\sigma}_{max}$	2.13×10^3	8	45	266	1.76	0.110	
$\widehat{\sigma}_{min}$	1.36×10^3	8	45	170	3.33	0.005	⋆
$\bar{\sigma}_{vm}$	29.1	8	45	3.62	1.84	0.094	⋆
$\bar{\sigma}_{max}$	4.28	8	45	0.53	0.80	0.607	
$\bar{\sigma}_{min}$	17.6	8	45	2.20	3.32	0.005	⋆
$\widehat{\epsilon}_{max}$	0.021	8	45	0.002	1.38	0.233	
$\widehat{\epsilon}_{min}$	0.026	8	45	0.003	2.43	0.028	⋆
$\bar{\epsilon}_{max}$	2.098×10^{-7}	8	45	2.62×10^{-8}	0.82	0.589	
$\bar{\epsilon}_{min}$	1.87×10^{-7}	8	45	2.34×10^{-8}	0.53	0.827	
V_f	6.52×10^7	8	45	8.15×10^7	0.99	0.459	
R	2.07×10^6	8	45	2.59×10^5	1.89	0.086	
R_u	6.82×10^6	8	45	8.52×10^5	0.65	0.730	

(a) Sum of squared deviations from mean values (between groups): $\sum_{i=0}^{n}(y_i - \bar{y})^2$.
(b) Degrees of freedom between groups.
(c) Degrees of freedom within groups.
(d) Mean of square (between groups): SS_b/df_b.
(e) F statistic: MS_b/MS_w.
(f) Significance level: $p < 0.05$.
∗ $(\bullet)_b$ and $(\bullet)_w$ denote *between* and *within* groups statistics.

Appendix B. Results of the statistical analyses for loading modes comparison.

Table B.6
One-way MANOVA results for loading modes comparison. Dependent variables employed were $\widehat{\sigma}_{vm}, \widehat{\sigma}_{max}, \widehat{\sigma}_{min}$.

Test Statistic	**Value**	$F^{(a)}$	$df_b{}^{(b)}$	$df_w{}^{(c)}$	**p-value**	**significance**$^{(d)}$
Pillai's Trace	0.538	2.098	15	144	0.013	⋆
Wilks' Lambda	0.529	2.200	15	127	0.009	⋆
Hotelling's Trace	0.764	2.276	15	134	0.007	⋆
Roy's Largest Root	0.557$^{(e)}$	5.347	5	48	0.001	⋆

(a) F statistic: MS_b/MS_w.
(b) Degrees of freedom between groups.
(c) Degrees of freedom within groups.
(d) Significance level: $p < 0.05$.
(e) The statistic is an upper bound on F that yields a lower bound on the significance level.
$*$ $(\bullet)_b$ and $(\bullet)_w$ denote *between* and *within* groups statistics.

Table B.7
One-way ANOVA results for loading modes comparison.

Factor	$SS_b{}^{(a)}$	$df_b{}^{(b)}$	$df_w{}^{(c)}$	$MS_b{}^{(d)}$	$F^{(e)}$	**p-value**	**significance**$^{(f)}$
$\widehat{\sigma}_{vm}$	1.75×10^3	5	48	349	0.53	0.751	
$\widehat{\sigma}_{max}$	1.09×10^3	5	48	219	1.35	0.26	
$\widehat{\sigma}_{min}$	800	5	48	160	2.69	0.032	⋆
$\bar{\sigma}_{vm}$	23.8	5	48	4.75	2.43	0.048	⋆
$\bar{\sigma}_{max}$	8.88	5	48	1.78	3.33	0.011	⋆
$\bar{\sigma}_{min}$	8.21	5	48	1.64	2.01	0.093	
$\widehat{\epsilon}_{max}$	0.006	5	48	0.001	0.92	0.476	
$\widehat{\epsilon}_{min}$	0.006	5	48	0.001	0.66	0.656	
$\bar{\epsilon}_{max}$	4.55×10^{-7}	5	48	9.10×10^{-8}	3.66	0.007	⋆
$\bar{\epsilon}_{min}$	8.34×10^{-7}	5	48	1.67×10^{-7}	5.97	< 0.001	⋆
V_f	3.11×10^7	5	48	6.21×10^6	0.73	0.601	
R	3.27×10^6	5	48	6.53×10^5	6.3	< 0.001	⋆
R_u	2.31×10^7	5	48	4.63×10^6	5.22	< 0.001	⋆

(a) Sum of squared deviations from mean values (between groups): $\sum_{i=0}^{n}(y_i - \bar{y})^2$.
(b) Degrees of freedom between groups.
(c) Degrees of freedom within groups.
(d) Mean of square (between groups): SS_b/df_b.
(e) F statistic: MS_b/MS_w.
(f) Significance level: $p < 0.05$.
$*$ $(\bullet)_b$ and $(\bullet)_w$ denote *between* and *within* groups statistics.